High Performance Self-Powered Photodetectors Based on Graphene Nanoribbons/Al_2O_3/InGaZnO Heterojunctions

Xiaoling Ye, Xiaoxiao Zheng, Lei Han, Yu Sun, Liang Wang, Ziheng Li, Wencheng Liu, Benqing Liu, Nan Han, Safia Khan, Syed Hassan Mujtaba Jafri, Mingyang Wang, Yafei Ning, and Hu Li

***Abstract*—Self-powered photodetectors which operate without external power sources hold immense promise in future photodetection systems. To achieve high-performance self-powered optoelectronic devices, efficient electron-hole pair separation is critical to generate high photocurrents. In this work, we successfully synthesized semiconducting graphene nanoribbons (GNRs) with a direct bandgap of 1.80 eV and employed them to construct a high-performance GNR/Al_2O_3/IGZO heterostructure photodetector. The built-in electric field in the heterojunctions enables this photodetector to exhibit remarkable performance, showing a responsivity of up to 68 mA/W, a detectivity of 8.34 $\times$ 10^{10} Jones, and rapid response times of 21/20 ms at zero bias. Furthermore, the photodetector features a wide spectral detection range of 405 to 1550 nm. These results highlight the promising potential of GNR/IGZO p-n heterojunction-based self-powered photodetectors in optoelectronic applications.**

***Index Terms*—Graphene nanoribbons, heterojunctions, responsivity, self-powered photodetectors.**

I. Introduction

DUE to the capability to convert optical signals into electrical signals, photodetectors have demonstrated wide applications in video imaging, optical communications, biomedical imaging and motion detection [1], [2], [3], [4]. Notably, self-powered photodetectors capable of efficient photodetection without any external power sources have attracted much attention from many researchers [5], [6], [7]. These devices often utilize Schottky photodiodes, which commonly operate in either the photovoltaic mode (zero-biased) or photoconductive mode (reverse-biased) [8], [9]. Self-powered photodetectors based on p-n junctions possess many advantages, such as low-cost fabrication, simple structures, compatibility with CMOS technology, self-powered operation, and broadband photodetection [10], [11].

In recent years, two-dimensional materials have provided a novel research platform for developing higher-performance self-powered photodetectors. Among these materials, graphene is considered as one of the most promising candidates for next-generation optoelectronic devices owing to its unique electrical, optical, and thermal properties [12], [13]. However, the primary challenges in developing graphene-based photodetectors originate from its inherent properties such as low absorption coefficient, zero bandgap, lack of gain mechanisms, and ultrafast carrier recombination in picoseconds [14], [15]. As a result, pure graphene-based photodetectors exhibit significantly low photoresponsivity, often just a few mA/W [16].

To improve the photoresponsivity of graphene-based photodetectors, researchers have explored the integration of graphene with three-dimensional semiconductors, including Si, InGaZnO (IGZO), GaN, ZnO, GaAs, and Ge, to create heterojunctions [17], [18], [19], [20]. These heterojunctions exhibit substantial photovoltaic effects, offering a potential solution to enhance the overall performance of photodetection. The straightforward fabrication of graphene/semiconductor heterostructures has spurred a research boom since 2010. In 2017, Li et al. created a self-powered photodetector with a broad response from ultraviolet (260 nm) to infrared (900 nm) by depositing a perovskite layer on graphene. The photodetector exhibited a responsivity of 0.375 A/W, a detectivity of 10^{11} Jones, and a signal-to-noise ratio of 4 $\times$ 10^6 [21]. In 2020, Won et al. utilized a graphene/hexagonal boron nitride (hBN)/Si structure to fabricate a self-powered van der Waals heterojunction photodetector which is sensitive to visible light. Their results demonstrated that

Manuscript received 15 March 2024; accepted 20 March 2024. Date of publication 26 March 2024; date of current version 19 April 2024. This work was supported in part by Shandong Provincial Natural Science Foundation under Grant ZR2022ZD05 and Grant ZR2021QE148, in part by the Shandong Provincial Natural Science Foundation for Excellent Young Scientists Fund Program (Overseas) under Grant 2022HWYQ-060, in part by the Guangdong Basic and Applied Basic Research Foundation under Grant 2022A1515011473 and Grant 2023A1515011218, in part by the Guangdong International Science and Technology Cooperation Program under Grant 2023A0505050087, and in part by Shenzhen Fundamental Research Program under Grant JCYJ20230807094119040. *(Corresponding authors: Hu Li; Yafei Ning; Mingyang Wang.)*

Xiaoling Ye, Xiaoxiao Zheng, Lei Han, Yu Sun, Liang Wang, Ziheng Li, Wencheng Liu, Benqing Liu, Nan Han, Safia Khan, and Mingyang Wang are with the Shandong Technology Centre of Nanodevices and Integration, School of Integrated Circuit, Shandong University, Jinan 250101, China (e-mail: mingyangwang@mail.sdu.edu.cn).

Syed Hassan Mujtaba Jafri is with the Department of Electrical Engineering, Mirpur University of Science and Technology, Mirpur Azad, Jammu and Kashmir 10250, Pakistan, and also with the Department of Materials Science and Engineering, Uppsala University, 75121 Uppsala, Sweden.

Yafei Ning and Hu Li are with the Shandong Technology Centre of Nanodevices and Integration, School of Integrated Circuit, Shandong University, Jinan 250101, China, and also with the Shenzhen Research Institute of Shandong University, Shenzhen 518063, China (e-mail: ningyafei@sdu.edu.cn; hu.li@sdu.edu.cn).

Digital Object Identifier 10.1109/JPHOT.2024.3381440

incorporating a thin hBN layer enables the design of asymmetric carrier transport and alleviates interfacial layer coupling [22]. Furthermore, other insulating layers including aluminum oxide (Al_2O_3), hafnium dioxide (HfO_2) can also be employed as the interface layer in graphene-based heterojunctions [23], [24]. In graphene-based van der Waals heterostructures, differing Fermi energy levels between graphene and semiconductors generate built-in electric fields once thermal equilibrium is achieved. These built-in electric fields provide a rectifying effect, evidenced by the asymmetric current-voltage (I-V) curves of the graphene/GaAs heterostructure [25].

In this work, a self-powered photodetector based on GNR/Al_2O_3/IGZO heterojunction is demonstrated. The heterojunction was created by transferring GNR films onto an n-type IGZO film and inserting a thin Al_2O_3 layer between GNR and IGZO to increase the interfacial barrier and reduce dark current. This structure promotes efficient photovoltaic conversion and rapid response, with light absorption and carrier separation primarily occurring near the heterojunction. The device displays a responsivity of 68 mA/W, a detectivity of 8.34×10^{10} Jones, and a rise/decay time of 21/20 ms at zero bias. Additionally, the photodetector offers a broad spectral detection capability (405–1550 nm). These findings suggest the GNR/Al_2O_3/IGZO heterojunction as a promising option for high-performance, low-cost self-powered photodetectors.

II. Materials and Methods

A. Fabrication of GNRs

Initially, 50 mg of single-walled carbon nanotubes (SWCNTs, M2013L4, Ossila) was heated at 300 °C for 30 minutes in ambient air. They were immersed in 50 mL of 98% sulfuric acid (H_2SO_4, Macklin) for 2 hours. Subsequently, 25 mg of potassium permanganate ($KMnO_4$, Sigma Aldrich) was added and stirred at 45 °C for 50 minutes until completely consumed. Then, the solution was poured into 200 mL of ice-cooled deionized water, and the reacted SWCNTs were separated by filtration through a 0.22 μm polytetrafluoroethylene membrane (Whatman). The post-reaction SWCNTs were thoroughly washed with deionized water and air-dried. To fully unzip SWCNTs, 20 mg of them was dispersed in 200 mL of a 1% sodium dodecyl benzene sulfonate (SDBS, Sinopharm) solution and subjected to 60 minutes of ultrasonication. Finally, the solution was washed with deionized water to eliminate SDBS.

B. Device Fabrication

The process flow of a heterojunction photodetector based on GNR/Al_2O_3/IGZO is shown in Fig. 3(a). The silicon dioxide substrate was initially cleaned by acetone, ethanol, and deionized water, followed by drying with nitrogen gas. Subsequently, an 80 nm-thick IGZO film was deposited onto a silicon wafer. Then, a 5 nm-thick layer of Al_2O_3 was grown on the IGZO film using atomic layer deposition. Next, the GNR film was transferred onto the Al_2O_3 layer. Finally, Ti/Au (20/50 nm) electrodes were deposited on the GNR film and the IGZO surface. The active area of the device is 0.096 mm^2.

The transfer process of the GNR films is illustrated in Fig. 2(a). First, GNR solution was deposited onto a nitrocellulose membrane filter (0.22 μm, Whatman). Subsequently, the GNR-loaded membrane was affixed to the surface of Al_2O_3 using deionized water. Next, acetone was slowly dripped onto the membrane until nitrocellulose membrane was completely dissolved. The sample was dried in air for 1 hour and then annealed at 300°C for 3 hours under a 5% Ar/H_2 atmosphere.

C. Structural Characterization

The Raman and Photoluminescence (PL) spectra were obtained using a RENISHAW Invia instrument with a 532 nm laser. The structural properties of GNRs and Cross-sectional images of the device were performed employing the FEI Talos F200X transmission electron microscope (TEM), while surface morphology was characterized by the FEI Strata DB235 field emission scanning electron microscope (SEM). The edge roughness of GNR films was measured by an atomic force microscope (AFM, CSPM5500). The SDR851 desktop optical transmittance measurement instrument was employed to measure the transmittance of GNR films. The thickness of GNR film was measured using a stylus profiler (DektakXT). The I-V characteristics of the devices were measured using an Agilent 2902A. To evaluate optoelectronic performance, the device was tested under laser illumination with 405 nm, 635 nm, 980 nm, 1550 nm wavelength. The laser power density was determined by using an Ophir Nova II optical power meter.

III. Results and Discussion

GNRs are synthesized by a solution-based process, as shown in Fig. 1(a). Initially, defects were introduced at the edges of SWCNTs using potent oxidizing agents. In this work, H_2SO_4 and $KMnO_4$ were employed to oxidize SWCNT edges [26], [27]. The ultrasonic process then unzipped SWCNTs along these defects to form GNRs. Details of methods are available in the Materials and Methods section. Unlike conventional GNR exfoliation techniques, our method precisely controls the oxidant amount to maintain a relatively low oxidation level. Furthermore, a crucial aspect of this experiment lies in dispersing SWCNTs in a solution to control their unzipping process. Due to their self-assembly traits, SWCNTs, with hydrophobic surface groups, tend to aggregate in liquids, hindering their dispersion. Hence, surfactants are often employed to improve SWCNT dispersibility [27]. This study selected SDBS to disperse SWCNTs in water. The hydrophobic alkyl chains of SDBS can adsorb onto the surface of SWCNT, while the hydrophilic groups can cover the nanotube surface. This enables SWCNTs to detach from aggregates and successfully disperse in the solution. Residual SDBS in GNR films may impair the performance of photodetectors. Specifically, remnants of SDBS are likely to alter film's conductivity and surface roughness, as well as potentially introduce scattering centers, which would decrease carrier lifetime and mobility, thereby reducing the photodetector's responsivity [28], [29], [30], [31]. Therefore, effectively removing SDBS is crucial for optimizing performance. In this work, we performed multiple rounds of vacuum filtration washing on the SDBS-containing

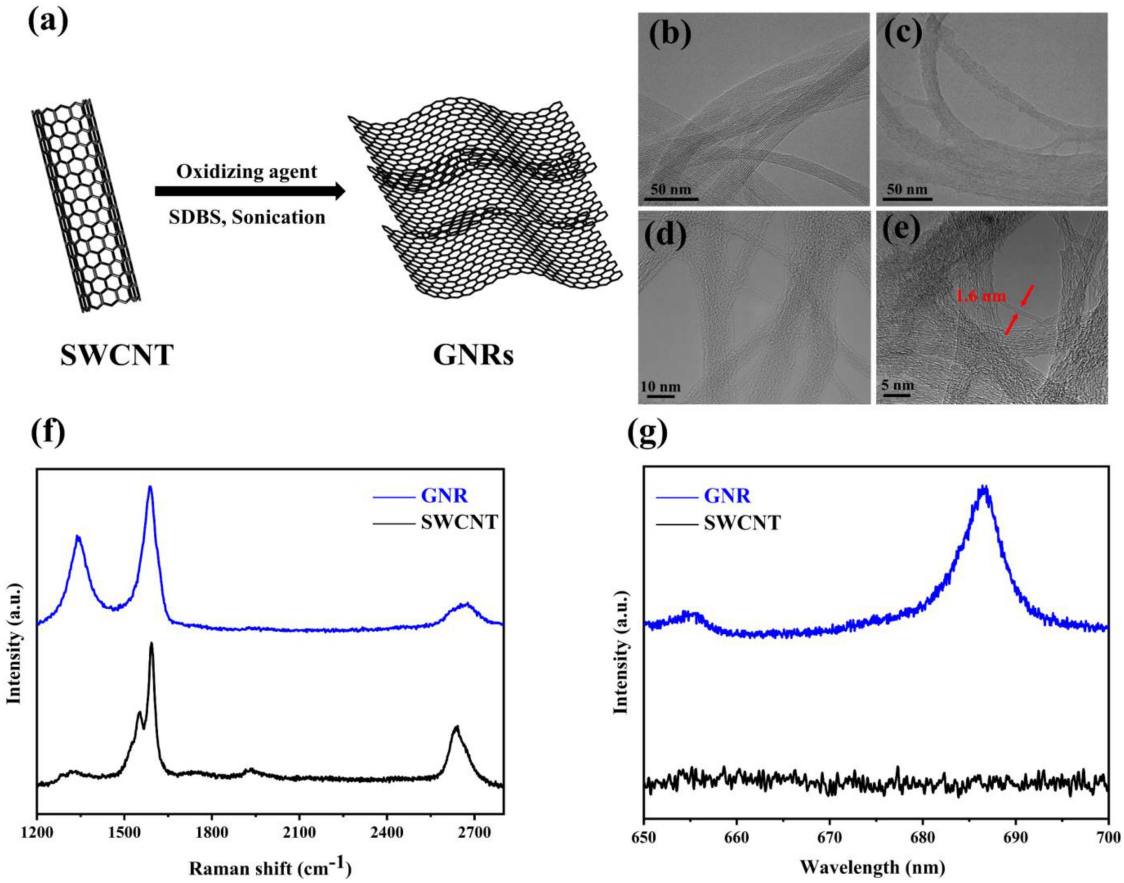

Fig. 1. (a) Schematics of the unzipping process from SWCNTs to GNRs. TEM images of (b) pristine SWCNT, (c) and (d) GNRs (e) a single GNR in the width of 1.6 nm (red arrow). (f) Raman spectra of SWCNTs and GNRs. (g) PL spectrum of SWCNT and GNR.

GNR films to eliminate SDBS as much as possible. Although trace amounts of SDBS might remain after the vacuum filtration, a subsequent annealing process at 300 °C for 3 hours in an Ar/H_2 atmosphere also effectively evaporates any residual SDBS.

TEM was employed to investigate the structural properties of GNRs. Fig. 1(b)–(e) displays four TEM images at different magnifications. As depicted in Fig. 1(b), SWCNTs are tightly assembled, featuring smooth edges due to their perfect geometric topology. Fig. 1(c)–(e) illustrate the structural features of strip-shaped GNRs. Unlike the orderly stacking observed in SWCNTs, the irregular edges of GNRs present an impediment to achieving similar dense packing. This structural difference between SWCNTs and GNRs is evident. The figures show GNR bundles with wavy boundaries, featuring gaps or overlaps. A single GNR's width, about 1.6 nm as indicated by the red arrow in Fig. 1(e), is smaller than SWCNTs' circumferences, which range from 3 to 5 nm. This implies that one SWCNT can break down into several GNRs. The disintegration mechanism, involving the formation of numerous structural defects on a SWCNT, accounts for this. During disintegration, a SWCNT may split in irregular directions, resulting in GNRs with rough edges and random structures.

Raman spectroscopy was employed to further characterize GNRs. Previous studies identified three Raman peaks in typical GNRs at 1350 cm^{-1} (D), 1600 cm^{-1} (G or D'), and 2700 cm^{-1} (G') [32], [33]. The G peak results from the stretching vibration of equivalent C-C bonds, whereas the G' peak arises from non-equivalent C-C bonds [33]. Structural defects cause the D peak, and inter-structural stress or phonons result in the D' peak [33]. Moreover, the relative intensities of these peaks may vary with the sample's morphology, orientation, and the substrate used in Raman measurements. Fig. 1(f) shows the Raman spectra of GNRs and pristine SWCNTs on the SiO_2 substrate. GNRs and SWCNTs both display the G peak at 1580 cm^{-1}, but only GNRs exhibit the D peak at 1350 cm^{-1}, indicating that defects arise from the dissociation of SWCNTs. The relative intensities of GNRs' peaks vary with the preparation method. Our results align with findings on chemically dissociated GNRs, confirming successful preparation through gentle chemical dissociation [34], [35]. In GNR samples, the G peak at 1580 cm^{-1} and the G' peak at 2690 cm^{-1} are characteristic of the in-plane vibration of sp^2 atom in graphene, which is sensitive to the number of graphene layers [36], [37]. The ratio of G' to G peak intensities ($I_{G'}/I_G$) serves as an identifier for monolayer graphene, where a value near or above 2 often indicates high-quality, defect-free [38]. Notably, the intensity of the G peak consistently surpasses that of the G' peak in GNR samples, suggesting that GNRs are multi-layered. PL characterization, a rapid and efficient method,

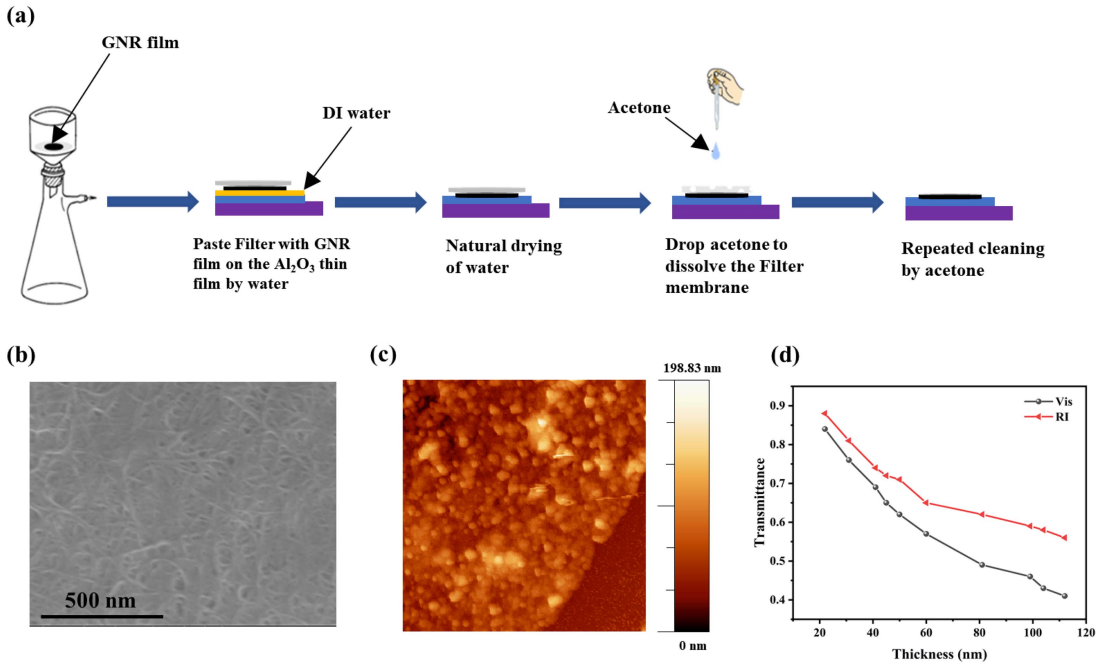

Fig. 2. Transfer and characterization of GNRs transparent film. (a) Schematic diagram of suction filtration fabricated GNR thin film. (b) SEM characterization of GNR films. (c) AFM characterization of GNRs film on SiO_2 substrate. (d) Transmittance results of GNRs film.

was used to investigate semiconductor behaviors in GNRs [39]. The semiconductor band gap is determined by (1):

$$E = \frac{hc}{\lambda} \tag{1}$$

where c, h, λ represents the velocity of light in vacuum, Planck constant and wavelength, respectively. The PL spectrum of GNRs shows a peak at 685 nm, not found in SWCNTs, indicating a semiconducting band gap of 1.80 eV in GNRs (Fig. 1(g)). These results align with our previous reports [34], [40].

GNR films were fabricated through a membrane adsorption filtration-dissolution technique, illustrated in Fig. 2(a). Initially, a solution containing GNRs was deposited on a filtration membrane to form a thin film through adsorptive filtration. The film was then transferred onto the Al_2O_3 surface. Finally, acetone was used to dissolve the filtration membrane, enabling efficient separation of the GNR films. The quality of the GNR film greatly depends on the deposition process. The SEM image in Fig. 2(b) shows the GNRs tightly packed and intertwined to form a film. The disordered configuration guarantees that GNR-based transparent films have uniform optical and electrical properties, as well as significant mechanical strength [41]. AFM was employed to investigate film edges, as depicted in Fig. 2(c). The deep red area in the image represents the silicon dioxide surface. The edge thickness of the GNRs film was measured to be approximately 50 nm. The film exhibited non-uniformity, as evidenced by the presence of small visible pin-holes.

Fig. 2(d) shows optical transmittance measurements across various wavelengths. The visible light (Vis) wavelength ranges from 380 to 760 nm, and the infrared light (IR) wavelength is at 940 nm. A negative correlation exists between GNR film thickness and transmittance. Notably, the peak transmittance of visible light can reach approximately 85% at a film thickness of around 20 nm, gradually decreasing to 40% at 113 nm. Another observation is that the transmittance of infrared light consistently exceeds that of visible light across all samples. There is a consistent decrease in overall absorption intensity with increasing wavelength, revealing a clear positive correlation between wavelength and transmittance. These optical properties can be attributed to graphene's two-dimensional structure and its molecular vibrational modes. On the one hand, this unique configuration offers a relatively larger surface area, creating numerous interfaces and scattering sites that notably facilitate the scattering and transmission of infrared light [41]. On the other hand, graphene's molecular vibration modes exhibit higher responsiveness to infrared light, further enhancing its transmission [42]. The peak transmission of infrared and visible light at 20 nm thickness is comparable to the transparency of commercial films like indium-tin-oxide, polyethylene terephthalate, and polycarbonate. Furthermore, the pronounced photoresponse in GNR/Al_2O_3/IGZO photodetectors primarily stems from light absorption in the GNR layer [43]. GNR films that are too thin compromise their light absorption capability, thus reducing the device's responsivity. On the other hand, overly thick GNR films lead to an increase in residual conductive metallic SWCNTs, which in turn, results in a higher dark current.

Fig. 3(a) presents the fabrication process schematic for the GNR/Al_2O_3/IGZO heterojunction photodetector. GNRs and device fabrication methods are detailed in the Materials and Methods section. GNR films were transferred via the previously described film-assisted filter dissolution technique. Fig. 3(b) shows the optical image of the heterojunction photodetector. The central region of the film has a thickness below 30 nm, while the periphery ranges from 30 nm to 60 nm. The

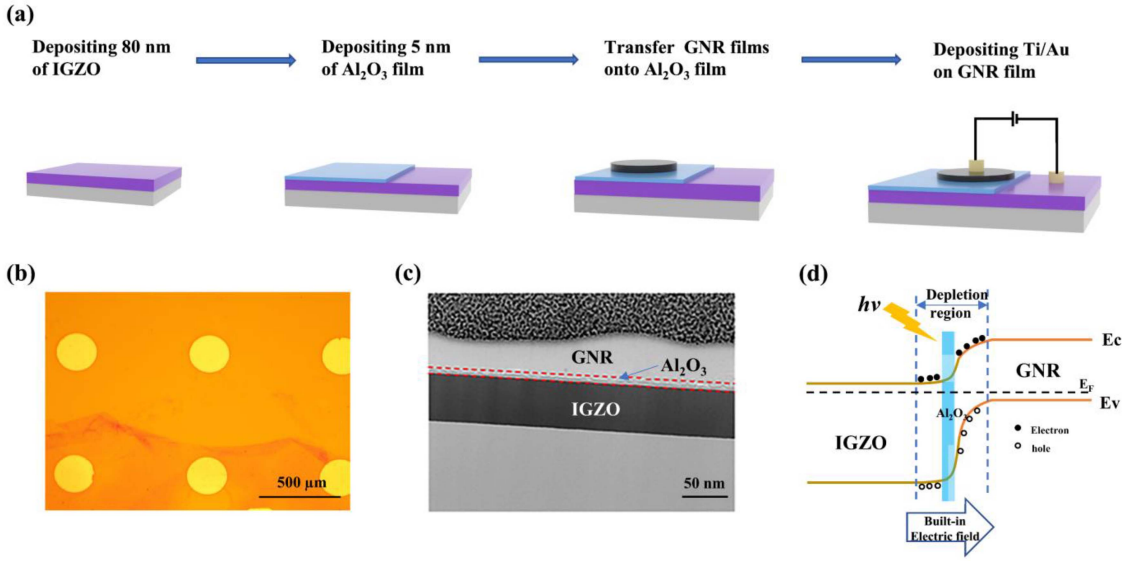

Fig. 3. (a) Process flow of GNR/Al_2O_3/IGZO photodetectors. (b) Optical image of GNR/Al_2O_3/IGZO heterojunction photodetector. (c) Cross-sectional TEM image of the fabricated device. (d) Schematic representation of the energy band diagram of the GNR/Al_2O_3/IGZO device under illumination.

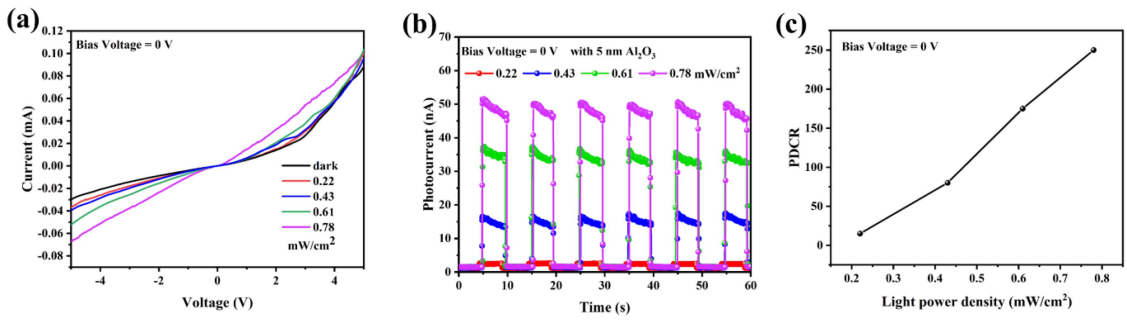

Fig. 4. Zero-bias photoelectric response of the GNR/Al_2O_3/IGZO-based photodetector. (a) I–V curves of GNR/Al_2O_3/IGZO structure in dark and under 635 nm light illumination. (b) Time dependent photoresponse of the photodetector under 635 nm light at 0 V bias. (c) PDCR as a function of the light power density under zero bias.

cross-sectional image of the fabricated GNR/Al_2O_3/IGZO heterojunction device is shown in Fig. 3(c). Fig. 3(d) illustrates the energy band diagram of the GNR/Al_2O_3/IGZO heterojunction, highlighting the generation, separation, and recombination of electron-hole pairs under 635 nm laser illumination. Electrons diffuse from the IGZO layer to the GNR layer, and holes move in the opposite direction, forming a depletion region at the interface when thermal equilibrium is achieved. This results in an inherent electric field directed from IGZO to GNR. In theory, photo-generated carriers are separated by built-in electric field, with photo-generated holes flowing towards the GNR side, and photo-generated electrons moving towards the IGZO side, thus generating photocurrent. However, in practical GNR/IGZO devices, the non-dense surface of the GNR films and the residual highly conductive SWCNTs create numerous reverse current leakage pathways, resulting in high dark current. Conversely, in GNR/Al_2O_3/IGZO devices, the Al_2O_3 interface layer serves as a Schottky barrier, effectively blocking leakage paths and facilitating efficient hole tunneling, thus enhancing photocurrent generation [24], [44]. The reduced reverse current through the Al_2O_3 barrier lowers hole density in the GNR valence band. In addition, the GNR with an open bandgap plays a key role in photon absorption, enhancing photodetection performance [43].

Fig. 4(a) shows the I-V curve of the GNR/Al_2O_3/IGZO device under dark and 635 nm laser irradiation. In dark conditions, the device exhibits typical rectifying characteristics, indicating a successful p-n junction formation between GNR and IGZO. The I-V characteristics of the device were investigated under laser illumination at intensities ranging from 0.22 mW/cm^2 to 0.78 mW/cm^2. The reverse current of the device increases with light intensity. However, without the Al_2O_3 interfacial layer, the GNR/IGZO heterojunction exhibited almost no rectifying behavior in the I-V curves within the applied bias range of -5 to +5 V (Fig. S1). This may be attributed to the incomplete dissociation of SWCNTs, with residual conductive metallic SWCNTs in the GNR film causing significant reverse currents. The photoresponse of the GNR/Al_2O_3/IGZO heterojunction photodetector under 635 nm light (0.22 to 0.78 mW/cm^2) is shown in

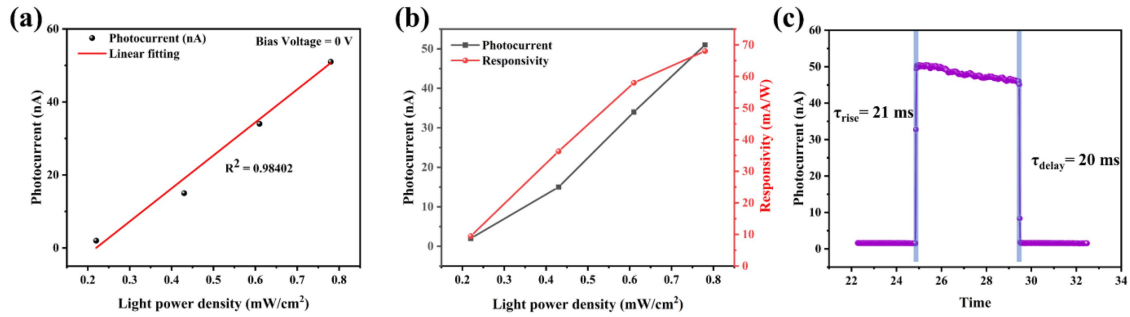

Fig. 5. (a) The photocurrents dependence of the light power density measured at 0 V. (b) The photocurrent and responsivity value of the GNR/Al_2O_3/IGZO photodetector at different light intensity. (c) Extraction of the rise/decay times of the photodetector.

Fig. 4(b). The magnitude of the device's photoresponse current demonstrates a certain positive correlation with the incident light power at zero bias, indicating excellent self-powering capability. The time response curve tends to be rectangular shape without significant attenuation during multiple alternating periods of light and dark, indicating the device's consistent repeatability.

To evaluate the influence of Al_2O_3 layer thickness on the GNR/Al_2O_3/IGZO device performance, dynamic current-time analyses were conducted for devices with Al_2O_3 layers of 0 nm, 2.5 nm, 5 nm, and 7.5 nm, as shown in Fig. 4(b) and Fig. S2a-c. Without the Al_2O_3 layer, the device exhibited negligible photocurrent when the laser was turned on (Fig. S2a). However, under the same illumination intensity, the device with a 5 nm Al_2O_3 layer demonstrated both higher photocurrent and lower dark current, significantly outperforming the devices with 2.5 nm and 7.5 nm layers, as shown in Fig. S2c. The superior performance of the 5 nm Al_2O_3 layer can be attributed to its reduction of direct contact between GNR and IGZO, minimizing undesirable electron tunneling and enhancing photoexcited charge carrier transport, thereby increasing photodetector sensitivity [45], [46]. Additionally, the thickness of 5 nm Al_2O_3 offers an optimized path for charge carrier transport that blocks unnecessary current pathways without excessively hindering the transport of charge carriers, optimizing photoelectric conversion efficiency [47], [48].

The photocurrent-to-dark-current ratio (PDCR) is defined as the ratio between photocurrent density (J_p) and the dark current density (J_d), which can be expressed by the following formula [42]:

$$\mathrm{PDCR} = \frac{|J_p - J_d|}{|J_d|} \tag{2}$$

In GNR/Al_2O_3/IGZO devices, the PDCR as a function of the light power density at a bias of 0 V is illustrated in Fig. 4(c). At a bias of 0 V and a light power density of 0.78 mW/cm^2, the highest PDCR value reached 250. Fig. 5(a) presents the dependency of the device's photocurrent on light power density, operating without external power sources. Linear regression analysis reveals a superior linear relationship ($R^2 = 0.98402$) under 0 V bias, implying that the observed photocurrent can reliably infer the light power density.

To quantitatively evaluate the optoelectronic performance of the GNR/Al_2O_3/IGZO heterojunction, three crucial parameters were assessed: photocurrent (I_p), photoresponsivity (R), and specific detectivity (D^*). These metrics are calculated using the following equations:

$$I_p = I_{ill} - I_d \tag{3}$$

$$R = \frac{|J_p - J_d|}{P} \tag{4}$$

$$D^* = \frac{R}{\sqrt{2eJ_d}} \tag{5}$$

where I_{ill}, I_d, P, e, are the current in illumination condition, dark current, light power density, elementary charge, respectively. In general, the responsivity of photodetectors serves as a measure of sensitivity, while detectivity reflects a photodetector's capability to discern faint optical signals [49]. Fig. 5(b) illustrates the relationship between incident light power density, photocurrent, and photoresponsivity. With an increase in incident light power density, the current density also increases, indicating a positive correlation between light power density and photocurrent. Across the light power density range of 0.22 to 0.78 mW/cm^2, the responsivity varies from 9.5 to 68.0 mA/W at zero bias. Based on the calculated formulas, a photoresponsivity of 68 mA/W and a detectivity of 8.34×10^{10} Jones were attained at a bias voltage of 0 V with an incident light intensity of 0.78 mW/cm^2.

Response time stands as another crucial metric for photodetectors. The rise time (τ_{rise}) represents the duration for the photocurrent to increase from 10% to 90% of the pulse peak, whereas the decay time (τ_{decay}) is correspondingly defined as the time taken for it to decrease from 90% to 10% [50]. As shown in Fig. 5(c), the GNR/Al_2O_3/IGZO photodetector exhibits remarkably swift response characteristics, with recorded rise and decay times of 21 ms and 20 ms, respectively. The rapid response is due to the robust built-in electric field at the GNR/IGZO interface, facilitating efficient separation of photo-generated carriers.

To assess the broad-spectrum detection capabilities of GNR/Al_2O_3/IGZO photodetector, dynamic current-time characteristics of the device were measured under various wavelength illuminations (405 - 1550 nm) at a light intensity of 0.78 mW/cm^2 and zero bias voltage (Fig. 6(a)). The 1.80 eV bandgap endows GNR with significant responsiveness to red light (e.g., 635 nm). Notably, the highest observe photocurrent is approximately 100 nA at 405 nm, exceeding that of 635 nm. This can be attributed to IGZO's wide bandgap, which

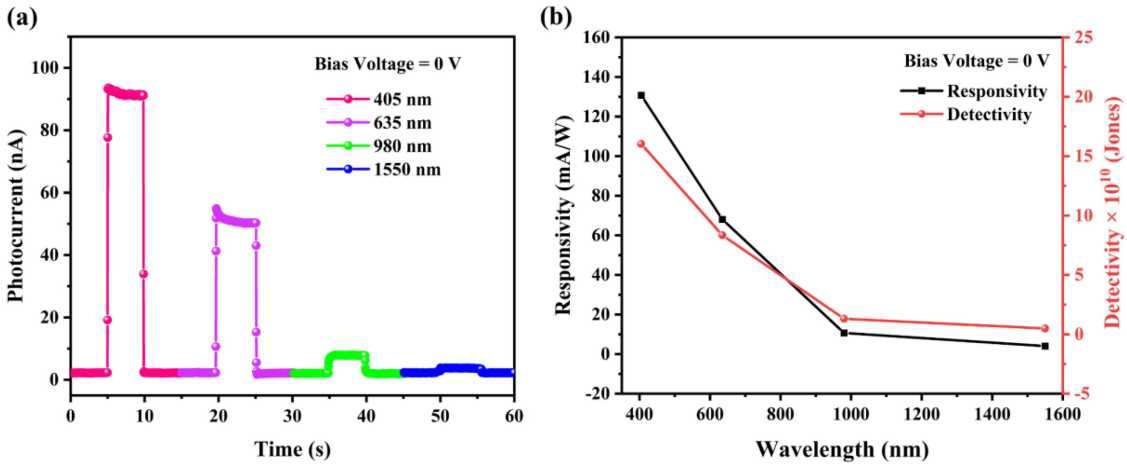

Fig. 6. (a) Time-dependent photocurrent curves for different wavelengths at 0 V bias voltage. (b) Calculated wavelength-dependent responsivity and detectivity.

TABLE I
PERFORMANCE COMPARISON OF GRAPHENE-BASED HETEROJUNCTION SELF-POWERED PHOTODETECTORS

Device structure	Responsivity	Detectivity	Response time	Ref.
GNR/Al$_2$O$_3$/InGaZnO	**68 mA/W**	**8.34×10^{10} Jones**	**21/20 ms**	**This work**
WSe$_2$-graphene-MoTe$_2$	40.84 mA/W	1.21×10^{11} Jones	468/428 μs	[51]
Graphene/GaAs nanowire	1.54 mA/W		71/194 μs	[52]
graphene/ZnO	50 μA/W		32 ms	[19]
MoS$_2$/graphene/GaAs	19.9 mA/W	4.86×10^{10} Jones	46.8/557 μs	[53]
ZnO NAs/graphene /Cu$_2$O	21.2 mA/W		0.6 ms	[54]
RbAg$_4$I$_5$ and graphene	20 mA/W		700 μs	[55]
TiO$_2$/graphene/ZnIn$_2$S$_4$ /electrolyte	13.79 mA/W		5/10 ms	[56]
Graphene/HfO$_2$/a-MoS$_2$	5.36 A/W		68 μs	[57]
Graphene/Si/graphene oxide	0.65 A/W		1 ms	[58]
graphene/MoSe$_2$/Au	89.5 mA/W	2.24 × 10^{10}	9.6 ms	[59]
ZnO/graphene/CdS/electrolyte	27.3 mA/W		5 ms	[60]
Graphene/Ge	1.27 A/W	9.6×10^9 Jones		[61]
Graphene/Si/Gd$_3$Fe$_5$O$_{12}$	0.9 A/W	1.35×10^{13} Jones	0.15 ms	[62]
graphene/Si	39.5 mA/W		5.0 μs	[63]

primarily responds to short-wave light [64], [65]. Furthermore, the higher energy of 405 nm light, compare to 635 nm, more readily excites electrons from the valence to conduction band, generating more carriers and increasing photocurrent [66], [67]. Fig. 6(b) illustrates the responsivity and detectivity of the GNR/Al$_2$O$_3$/IGZO device across a wide wavelength range from 405 to 1550 nm. At 0 V bias voltage, the photodetector shows responsivity of approximately 130.7, 68.0, 10.6, and 4.0 mA/W to 405, 635, 980, and 1550 nm illumination, respectively, along with detectivities of 1.6 × 10^{11}, 8.34 × 10^{10}, 1.30 × 10^{10}, and 4.9 × 10^9 Jones. Although responsivity at 980 - 1550 nm is lower, the capability to detect across a broad spectral range from ultraviolet to near-infrared qualifies it as a broad-band detector.

To highlight the superior performance of our GNR/Al$_2$O$_3$/IGZO heterojunction self-powered photodetector, we conducted a comparative analysis with other graphene-based heterojunction self-powered photodetectors previously reported in the literature, as detailed in Table I. This comparison reveals that the photodetectors utilizing GNR/Al$_2$O$_3$/IGZO heterojunctions outperform most existing graphene-based self-powered devices in terms of single or combined performance metrics.

IV. CONCLUSION

In summary, this study demonstrates a self-powered heterojunction photodetector utilizing a GNR/Al$_2$O$_3$/IGZO heterostructure. Within the device, photon absorption and carrier separation predominantly occur in the p-n junction region, facilitating efficient photoconversion and rapid response times. At zero bias, the device exhibits a responsivity of 68 mA/W, a detectivity of 8.34 × 10^{10} Jones and a rise/decay time of

21/20 ms. Additionally, the photodetector boasts a broad detection spectrum, ranging from 405 to 1550 nm. The enhancement in performance of the device can be primarily attributed to GNR's bandgap of 1.80 eV for photon absorption and the introduction of Al_2O_3 interfacial layer to raise the barrier height and significantly reduce dark current.

REFERENCES

[1] F. H. L. Koppens, T. Mueller, P. Avouris, A. C. Ferrari, M. S. Vitiello, and M. Polini, "Photodetectors based on graphene, other two-dimensional materials and hybrid systems," *Nature Nanotechnol.*, vol. 9, no. 10, pp. 780–793, Oct. 2014.

[2] F. Withers, T. H. Bointon, M. F. Craciun, and S. Russo, "All-graphene photodetectors," *ACS Nano*, vol. 7, no. 6, pp. 5052–5057, Jun. 2013.

[3] X. Ye et al., "Advances in the field of two-dimensional crystal-based photodetectors," *Nanomaterials*, vol. 13, no. 8, 2023, Art. no. 1379.

[4] Z. Li, T. Yan, and X. Fang, "Low-dimensional wide-bandgap semiconductors for UV photodetectors," *Nature Rev. Mater.*, vol. 8, no. 9, pp. 587–603, Sep. 2023.

[5] Z. Zhan, L. Zheng, Y. Pan, G. Sun, and L. Li, "Self-powered, visible-light photodetector based on thermally reduced graphene oxide–ZnO (rGO–ZnO) hybrid nanostructure," *J. Mater. Chem.*, vol. 22, no. 6, pp. 2589–2595, 2012, doi: 10.1039/C1JM13920G.

[6] L. Peng, L. Hu, and X. Fang, "Energy harvesting for nanostructured self-powered photodetectors," *Adv. Funct. Mater.*, vol. 24, no. 18, pp. 2591–2610, 2014.

[7] M. Deng, Z. Li, X. Deng, Y. Hu, and X. Fang, "Wafer-scale heterogeneous integration of self-powered lead-free metal halide UV photodetectors with ultrahigh stability and homogeneity," *J. Mater. Sci. Technol.*, vol. 164, pp. 150–159, Nov. 2023.

[8] A. Basir et al., "A novel self-powered photodiode based on solution-processed organic TPD:Alq3 active layer," *Mater. Sci. Semicond. Process.*, vol. 131, Aug. 2021, Art. no. 105886.

[9] Y. Chen, L. Su, M. Jiang, and X. Fang, "Switch type PANI/ZnO core-shell microwire heterojunction for UV photodetection," *J. Mater. Sci. Technol.*, vol. 105, pp. 259–265, Apr. 2022.

[10] H. Qiao, Z. Huang, X. Ren, S. Liu, Y. Zhang, and X. Qi, "Self-powered photodetectors based on 2D materials," *Adv. Opt. Mater.*, vol. 8, Sep. 2019, Art. no. 1900765.

[11] B. Zhao et al., "An ultrahigh responsivity (9.7 mA W−1) self-powered solar-blind photodetector based on individual ZnO–Ga2O3 heterostructures," *Adv. Funct. Mater.*, vol. 27, no. 17, 2017, Art. no. 1700264.

[12] C. - H. Liu, Y. - C. Chang, T. B. Norris, and Z. Zhong, "Graphene photodetectors with ultra-broadband and high responsivity at room temperature," *Nature Nanotechnol.*, vol. 9, no. 4, pp. 273–278, Apr. 2014.

[13] J. Li et al., "Metamaterial grating-integrated graphene photodetector with broadband high responsivity," *Appl. Surf. Sci.*, vol. 473, pp. 633–640, 2019.

[14] R. R. Nair et al., "Fine structure constant defines visual transparency of graphene," *Science*, vol. 320, no. 5881, pp. 1308–1308, 2008.

[15] H. Nan, R. Zhou, X. Gu, S. Xiao, and K. Ostrikov, "Recent advances in plasma modification of 2D transition metal dichalcogenides," *Nanoscale*, vol. 11, no. 41, pp. 19202–19213, 2019, doi: 10.1039/C9NR05522C.

[16] T. Mueller, F. Xia, and P. Avouris, "Graphene photodetectors for high-speed optical communications," *Nature Photon.*, vol. 4, no. 5, pp. 297–301, May 2010.

[17] A. Pelella, A. Grillo, E. Faella, G. Luongo, M. B. Askari, and A. Di Bartolomeo, "Graphene–silicon device for visible and infrared photodetection," *ACS Appl. Mater. Interfaces*, vol. 13, no. 40, pp. 47895–47903, Oct. 2021.

[18] C. Liu et al., "A nanopillar-modified high-sensitivity asymmetric graphene–GaN photodetector," *Nanoscale*, vol. 13, no. 41, pp. 17512–17520, 2021, doi: 10.1039/D1NR04102A.

[19] D. Chen et al., "Self-powered ultraviolet photovoltaic photodetector based on graphene/ZnO heterostructure," *Appl. Surf. Sci.*, vol. 529, Nov. 2020, Art. no. 147087.

[20] K. Y. Thai et al., "MoS2/graphene photodetector array with strain-modulated photoresponse up to the near-infrared regime," *ACS Nano*, vol. 15, no. 8, pp. 12836–12846, Aug. 2021.

[21] J. Li et al., "High-performance, self-powered photodetectors based on perovskite and graphene," *ACS Appl. Mater. Interfaces*, vol. 9, no. 49, pp. 42779–42787, Dec. 2017.

[22] U. Y. Won et al., "Efficient photovoltaic effect in graphene/h-BN/silicon heterostructure self-powered photodetector," *Nano Res.*, vol. 14, no. 6, pp. 1967–1972, Jun. 2021.

[23] S. - J. Jeong et al., "Thickness scaling of atomic-layer-deposited HfO2 films and their application to wafer-scale graphene tunnelling transistors," *Sci. Rep.*, vol. 6, no. 1, Feb. 2016, Art. no. 20907.

[24] C. Kim, T. J. Yoo, K. E. Chang, M. G. Kwon, H. J. Hwang, and B. H. Lee, "Highly responsive near-infrared photodetector with low dark current using graphene/germanium schottky junction with Al_2O_3 interfacial layer," *Nanophotonics*, vol. 10, no. 5, pp. 1573–1579, 2021.

[25] X. Li et al., "18.5% efficient graphene/GaAs van der Waals heterostructure solar cell," *Nano Energy*, vol. 16, pp. 310–319, Sep. 2015.

[26] M. J. Yoo and H. B. Park, "Effect of hydrogen peroxide on properties of graphene oxide in Hummers method," *Carbon*, vol. 141, pp. 515–522, Jan. 2019.

[27] D. Wei et al., "Controllable unzipping for intramolecular junctions of graphene nanoribbons and single-walled carbon nanotubes," *Nature Commun.*, vol. 4, no. 1, Jan. 2013, Art. no. 1374.

[28] V. Agarwal et al., "Influence of anionic surfactants on the fundamental properties of polymer/reduced graphene oxide nanocomposite films," *ACS Appl. Mater. Interfaces*, vol. 13, no. 15, pp. 18338–18347, Apr. 2021.

[29] Z. - Z. Gu, S. - L. Jia, G. Li, C. Li, Y. - Q. Wu, and H. - Z. Geng, "Mechanism of surface treatments on carbon nanotube transparent conductive films by three different reagents," *RSC Adv.*, vol. 9, no. 6, pp. 3162–3168, 2019.

[30] A. M. Ganose, J. Park, A. Faghaninia, R. Woods-Robinson, K. A. Persson, and A. Jain, "Efficient calculation of carrier scattering rates from first principles," *Nature Commun.*, vol. 12, no. 1, Apr. 2021, Art. no. 2222.

[31] S. Wang et al., "Effective lifetime of non-equilibrium carriers in semiconductors from non-adiabatic molecular dynamics simulations," *Nature Comput. Sci.*, vol. 2, no. 8, pp. 486–493, Aug. 2022.

[32] D. Rizzo et al., "Multiwavelength raman spectroscopy of ultranarrow nanoribbons made by solution-mediated bottom-up approach," *Phys. Rev. B*, vol. 100, no. 4, Jul. 2019, Art. no. 045406.

[33] L. M. Malard, M. A. Pimenta, G. Dresselhaus, and M. S. Dresselhaus, "Raman spectroscopy in graphene," *Phys. Rep.*, vol. 473, no. 5, pp. 51–87, Apr. 2009.

[34] H. Li et al., "Photoluminescent semiconducting graphene nanoribbons via longitudinally unzipping single-walled carbon nanotubes," *ACS Appl. Mater. Interfaces*, vol. 13, no. 44, pp. 52892–52900, Nov. 2021.

[35] L. Xie et al., "Graphene nanoribbons from unzipped carbon nanotubes: Atomic structures, raman spectroscopy, and electrical properties," *J. Amer. Chem. Soc.*, vol. 133, no. 27, pp. 10394–10397, Jul. 2011.

[36] R. Saito, M. Hofmann, G. Dresselhaus, A. Jorio, and M. S. Dresselhaus, "Raman spectroscopy of graphene and carbon nanotubes," *Adv. Phys.*, vol. 60, no. 3, pp. 413–550, Jun. 2011.

[37] M. Wall, "Raman spectroscopy optimizes graphene characterization," *Adv. Mater. Processes*, vol. 170, pp. 35–38, Apr. 2012.

[38] A. - S. Al-Sherbini, M. Bakr, I. Ghoneim, and M. Saad, "Exfoliation of graphene sheets via high energy wet milling of graphite in 2-ethylhexanol and kerosene," *J. Adv. Res.*, vol. 8, no. 3, pp. 209–215, May 2017.

[39] G. D. Gilliland, "Photoluminescence spectroscopy of crystalline semiconductors," *Mater. Sci. Eng.: R: Rep.*, vol. 18, no. 3, pp. 99–399, Mar. 1997.

[40] M. Wang et al., "High-performance photodetectors based on semiconducting graphene nanoribbons," *Nano Lett.*, vol. 24, pp. 165–171, Nov. 2023.

[41] J. Bai and Y. Huang, "Fabrication and electrical properties of graphene nanoribbons," *Mater. Sci. Eng.: R: Rep.*, vol. 70, pp. 341–353, Nov. 2010.

[42] Y. Qin et al., "Ultra-high performance amorphous Ga2O3 photodetector arrays for solar-blind imaging," *Adv. Sci.*, vol. 8, no. 20, 2021, Art. no. 2101106.

[43] M. Wang et al., "High-performance photodetectors based on semiconducting graphene nanoribbons," *Nano Lett.*, vol. 24, no. 1, pp. 165–171, Jan. 2024.

[44] S. Das, D. Pandey, J. Thomas, and T. Roy, "The role of graphene and other 2D materials in solar photovoltaics," *Adv. Mater.*, vol. 31, no. 1, 2019, Art. no. 1802722.

[45] F. P. García de Arquer, "Plasmonic hot-carrier optoelectronics," *ACS Nano*, vol. 14, pp. 9963–9971, 2015.

[46] M. L. Brongersma, "Plasmonic photodetectors, photovoltaics, and hot-electron devices," *Proc. IEEE*, vol. 104, no. 12, pp. 2349–2361, Dec. 2016.

[47] C. Battaglia, A. Cuevas, and S. De Wolf, "High-efficiency crystalline silicon solar cells: Status and perspectives," *Energy Environ. Sci.*, vol. 9, no. 5, pp. 1552–1576, 2016.

[48] W. Xu, Z. Wang, and A. T. Wee, "2 D material-based photodetectors for imaging," *Opt. Imag. Sens.: Mater., Devices Appl.*, vol. 2, pp. 11–54, 2023.

[49] W. Xin et al., "Low-dimensional-materials-based photodetectors for next-generation polarized detection and imaging," *Adv. Mater.*, vol. 36, 2023, Art. no. 2306772.
[50] C. Xie et al., "Core–shell heterojunction of silicon nanowire arrays and carbon quantum dots for photovoltaic devices and self-driven photodetectors," *ACS Nano*, vol. 8, no. 4, pp. 4015–4022, Apr. 2014.
[51] P. Feng et al., "A high-performance self-powered photodetector based on WSe2–graphene–MoTe2 van der waals heterojunctions," *J. Mater. Chem. C*, vol. 10, no. 24, pp. 9401–9406, 2022, doi: 10.1039/D2TC01441F.
[52] Y. Wu, X. Yan, X. Zhang, and X. Ren, "A monolayer graphene/GaAs nanowire array schottky junction self-powered photodetector," *Appl. Phys. Lett.*, vol. 109, no. 18, 2016, Art. no. 183101.
[53] J. Qu and J. Chen, "Graphene/GaAs schottky junction near-infrared photodetector with a MoS2 quantum dots absorption layer," *IEEE Trans. Electron Devices*, vol. 69, no. 8, pp. 4331–4336, Aug. 2022.
[54] Z. Bai, J. Liu, F. Liu, and Y. Zhang, "Enhanced photoresponse performance of self-powered UV–visible photodetectors based on ZnO/Cu2O/electrolyte heterojunctions via graphene incorporation," *J. Alloys Compounds*, vol. 726, pp. 803–809, Dec. 2017.
[55] P. Wang et al., "Enhanced self-powered ion-modulated photodetector based on an asymmetric composite structure of superionic conductor RbAg4I5 and graphene," *Opt. Exp.*, vol. 30, no. 23, pp. 41644–41657, Nov. 2022.
[56] X. Wang et al., "High performance self-powered UV–visible photodetectors based on TiO_2/graphene/ZnIn2S4/electrolyte heterojunctions," *Ceramics Int.*, vol. 48, no. 9, pp. 13090–13099, May 2022.
[57] Z. Huang et al., "Interfacial gated graphene photodetector with broadband response," *ACS Appl. Mater. Interfaces*, vol. 13, pp. 22796–22805, May 2021.
[58] Y. Wang, S. Yang, D. R. Lambada, and S. Shafique, "A graphene-silicon schottky photodetector with graphene oxide interlayer," *Sensors Actuators A: Phys.*, vol. 314, Oct. 2020, Art. no. 112232.
[59] B. Liu et al., "Self-powered and fast photodetector based on graphene/$MoSe_2$/Au heterojunction," *Superlattices Microstructures*, vol. 130, pp. 87–92, Jun. 2019.
[60] G. Huang, P. Zhang, and Z. Bai, "Self-powered UV–visible photodetectors based on ZnO/graphene/CdS/electrolyte heterojunctions," *J. Alloys Compounds*, vol. 776, pp. 346–352, Mar. 2019.
[61] M. Kwon et al., "Performance enhancement of graphene/ge near-infrared photodetector by modulating the doping level of graphene," *APL Photon.*, vol. 7, Jan. 2022, Art. no. 026101.
[62] P. Ji et al., "High-performance photodetector based on an interface engineering-assisted graphene/silicon schottky junction," *Microsystems Nanoeng.*, vol. 8, no. 1, Jan. 2022, Art. no. 9.
[63] C. Wang et al., "High responsivity and high-speed 1.55 μm infrared photodetector from self-powered graphene/Si heterojunction," *Sensors Actuators A: Phys.*, vol. 291, pp. 87–92, Jun. 2019.
[64] J. Chung, Y. J. Tak, W. - G. Kim, B. H. Kang, and H. J. Kim, "Artificially fabricated subgap states for visible-light absorption in indium–gallium–zinc oxide phototransistor with solution-processed oxide absorption layer," *ACS Appl. Mater. Interfaces*, vol. 11, no. 42, pp. 38964–38972, 2019.
[65] Y. Yuan et al., "Artificial leaky integrate-and-fire sensory neuron for in-sensor computing neuromorphic perception at the edge," *ACS Sensors*, vol. 8, pp. 2646–2655, 2023.
[66] J. Moffatt, G. Tsiminis, E. Klantsataya, T. de Prinse, D. Ottaway, and N. Spooner, "A practical review of shorter than excitation wavelength light emission processes," *Appl. Spectrosc. Rev.*, vol. 55, no. 4, pp. 327–349, 2020.
[67] A. J. Schmitt and S. P. Obenschain, "The importance of laser wavelength for driving inertial confinement fusion targets. II. target design," *Phys. Plasmas*, vol. 30, no. 1, 2023, Art. no. 012701.